www.nature.com/scientificreports

scientific reports

OPEN

Advanced stacked modeling techniques for material porosity estimation via high-resolution computed tomography imaging

Bubryur Kim[1], Sri Preethaa K.R.[2]✉, Yuvaraj Natarajan[2], Danushkumar[3], Sungwoo Park[4] & Sukhoon Pyo[5]

This study presents a deep convolutional neural network (DeepCNN) based framework for the automatic estimation of porosity in concrete materials from two-dimensional computed tomography (2D CT) scan images. Addressing the limitations of manual and time-consuming traditional porosity measurement methods, the proposed approach integrates advanced image processing techniques to improve robustness under low resolution and noisy imaging conditions. The DeepCNN architecture comprises a multi stage feature extractor with 21 convolutional layers and an SPP based neck, trained on 20,520 annotated CT images after data augmentation. Preprocessing steps include automated region of interest detection, intensity normalization, and class specific filtering prior to porosity estimation. The framework performs material classification and porosity estimation across multiple concrete classes, including cement-based mortars (CM0, CM5, CM10, CM20), geopolymer based mortar (GM), and ultra-high performance concrete (UHPC), using a rule based adaptive thresholding (RBAT) strategy incorporating clustering, filtering, and thresholding operations. Porosity is quantified by computing the ratio of pore area to the total image area. Across all material classes, the estimated porosity values showed close agreement with vacuum pycnometer measurements, with deviations within 2–3%, including deviations of 1.5% for UHPC and 1.3% for CM10. The DeepCNN classifier achieved a precision recall AUC of 1.0 during testing. These results demonstrate that the proposed hybrid framework provides an accurate, automated, and computationally efficient solution for porosity assessment, suitable for practical and industrial CT based material characterization workflows.

Keywords Porosity prediction, Convolution neural network, Stacked modeling, Vacuum pycnometer, Material characterization

Porosity, a fundamental material property, refers to the proportion of voids or empty spaces within a solid structure. It is essential for determining the overall performance and behavior of materials and their potential applications. Porosity also influences the mechanical strength, permeability, thermal insulation, and chemical reactivity of materials[1]. For instance, in civil engineering, the porosity of concrete material determines its strength and durability, whereas in the petroleum industry, the porosity of reservoir rocks directly impacts the amount of extractable oil or gas. In advanced materials science, porous structures are integral to the design of cutting-edge products, such as supercapacitors, drug delivery systems, and catalytic converters. Therefore, material porosity must be accurately determined for ensuring high product quality and better economic outcomes[2].

Image processing has emerged as a pivotal technique in assessing the porosity of materials, particularly with the introduction of cutting-edge imaging methods such as X-ray microtomography (μCT)[3] and scanning electron microscopy (SEM)[4]. The internal structure of a material can be studied using these methods, ensuring an accurate quantification of pore spaces[5,6]. First, three-dimensional (3D) structural images are acquired using μCT, high-resolution two-dimensional images are acquired using SEM, and images with more prominent,

[1]School of Space Engineering Sciences, Kyungpook National University, 80, Daehak-ro, Buk-gu, Daegu 41566, Korea. [2]School of Computer Science and Engineering, Vellore Institute of Technology, Vellore 632014, India. [3]Data Science and Artificial Intelligence, Eindhoven University of Technology (TU/e) Eindhoven, Eindhoven, The Netherlands. [4]School of Architecture & Building Science, Chung-Ang University, 84 Heukseok- ro, Dongjak-gu, Seoul 06974, Republic of Korea. [5]Department of Civil, Urban, Earth, and Environmental Engineering, National Institute of Science and Technology (UNIST), Ulsan 44919, Republic of Korea. ✉email: sripreethaa.kr@vit.ac.in

discernible pores are obtained using optical microscopy[7]. Then, preprocessing steps such as thresholding for partitioning the solid material surfaces and pores based on gray-scale intensity, filtering for minimizing image noise, and contrast enhancement for amplifying feature visibility are performed. Several thresholding methods such as Ostu[7], extended Ostu[8], histogram-based[9], and experimental-based are used on the CT-scan images for identifying the pores and solid areas. The resolution of μCT devices restricts the analysis of pore properties from the images; pores larger than the device resolution can be easily identified, whereas identifying smaller pores is challenging. To address this issue, a threshold is used. As structures are scale-dependent, they influence various material properties differently. Therefore, an appropriate and arbitrary threshold must be chosen, which can be varied based on the user and the acquired images[10], such as mercury intrusion porosity[11], volumetric analysis[12], and global thresholding[13] with local refinement methods. Although these thresholds provide realistic information about material structures, they require the segmentation of μCT images[14].

Image segmentation is performed for partitioning the solid structure and pore spaces using techniques such as region growing, watershed segmentation, and edge detection[15]. The segmented images are further refined by segregating or amalgamating image features by performing morphological operations such as erosion, dilation, opening, and closing[16]. Then, quantification is performed, wherein the porosity is calculated based on the pixel or voxel ratio and pore size distribution and pore interconnectivity, which can impact permeability are evaluated. Postprocessing techniques, particularly for 3D data, require 3D visualization tools such as volume rendering or skeletonization, to retain the material's actual physical structure. The accuracy of the porosity estimated using imaging technique is validated by comparing the results with those obtained via experiments or benchmarks. Phases such as pore space and solid grains in porous materials can be accurately differentiated by segmenting their gray-scale images. However, traditional methods require manual intervention, resulting in inherent biases and inconsistencies, and achieving precise multimineral segmentation is challenging[15–17]. Despite the advancements in imaging technology and computational power, several constraints persist such as challenges with balancing the image resolution and field of view (FOV). For instance, the quantification of sub-micrometer details of carbonated rocks is affected at large-scale due to rock heterogeneity[18]. Similarly, sub-micrometer fractures in delicate rock samples affect the resolution of images. This dichotomy between achieving high resolution and a wide FOV is as a fundamental limitation in imaging[19]. Large memory and high computational speeds are required for processing images with large dimensions. Although large simulations can be performed on workstations, image sizes surpassing model sizes are likely to endure due to the ongoing growth in imaging dimensions[20].

Machine learning and artificial intelligence have further revolutionized image processing. Advanced algorithms and neural networks are trained to autonomously segment images, thus reducing manual intervention and enhancing prediction accuracy. Image processing is a comprehensive, nondestructive technique for porosity estimation; however, meticulous calibration and validation and occasional manual oversight must be ensured to guarantee precise results, for which convolutional neural networks (CNNs) are used[21]. CNNs can learn from high-quality data, consider surrounding shapes and textures, and evolve in architecture to enhance image segmentation accuracy. Unlike traditional methods, CNNs do not rely on user-defined filters and statistical measures to capture surrounding information, yielding improved results[22]. Based on these findings, a CNN-based methodology is proposed herein to estimate the porosity of a material from a given 2D CT-scan image. The proposed methodology focuses on integrating techniques that can efficiently estimate porosity value using limited information about the material such as its CT scan image and class label.

Despite significant advances in image-based porosity analysis, several challenges still exist. The precise identification of pores is heavily reliant on picture quality, constraining the detection of intricate pore structures. Secondly, micro-computed tomography images are frequently influenced by noise, beam hardening, and reconstruction artifacts, which diminish segmentation reliability and often necessitate manual intervention. Third, fixed thresholding approaches have difficulties in generalizing across materials with varying microstructural and grayscale properties. These constraints highlight the importance for an automated and adaptive system that can accommodate material-specific variations while reducing user bias.

The novelty of this study is not the development of a fundamentally new deep learning architecture or segmentation method, but rather the application-driven design of a hybrid and completely automated porosity estimation framework customized for micro-CT images of cement-based and geopolymer materials. The uniqueness lies in the structured integration of an adapted convolutional neural network for material-aware ROI localization and classification with a domain-informed, rule-based adaptive thresholding technique for porosity measurement. Unlike end-to-end semantic segmentation approaches that require extensive pixel-level annotations and large training datasets, the proposed framework separates material identification and porosity estimation, allowing for interpretable, stable, and computationally efficient porosity assessment under practical imaging constraints. This design decision tackles frequent issues in industrial CT workflows, such as limited labeled data, diverse material classes, and the necessity for near real-time inference, providing a practical alternative to fully data-driven segmentation pipelines.

This article flow is organized as follows: Sect. 2 discusses the related research on machine learning techniques for porosity estimation and its challenges. Section 3 elaborates on the workflow of the proposed method detailing the DeepCNN architecture and rule-based adaptive threshold method. Section 4 validates the results obtained using the proposed method. Section 5 concludes the study and discusses the limitations as well as future prospects.

Related works

Various tools have been developed to evaluate the structural and transport properties of porous materials such as permeability, pore size, diffusivity, and porosity. Traditional methods such as empirical and numerical models analyze porous media using experimental parameters; however, they are time-consuming and their complexity increases with image scale[23]. Extensive data related to materials are now available due to advances in automation and computational power. Machine learning algorithms that can identify patterns within vast datasets have been developed[24]. In particular, deep learning (DL)-based CNNs are used for computing the properties of porous materials and extracting pertinent features from training data[25]. Several image-based machine learning tools, including gradient boosting regression (GDR) and support vector machines (SVM), have been applied to microscopic images of porous materials. Among them, GDR yields accurate predictions based on the physical descriptors used as inputs[26]. DL models classify images based on morphology and enhance image quality[27]. Szegedy et al. assessed pretrained DL models for classifying SEM images, among which Inception v3 exhibited the highest accuracy and efficiency but could not process atypical images[28]. Pixel-wise classification, offering detailed insights into object shapes, was superior to global image classification. Azimi et al. and DeCost et al. used specialized networks for segmenting and analyzing intricate microscopic components in materials such as carbon steel, showcasing the potency of well-designed networks in handling vast datasets[29–31].

A three-phase methodology for predicting porosity from X-ray μCT images of low-density ceramic materials was proposed, which used nonlocal denoising, CNN for pore segmentation, and quantitative analysis for 3D pore metrics, highlighting the shortcomings of traditional porosity estimation methods[32]. Predicting material properties, such as permeability, is challenging due to the complex nature of the microstructures of porous media. The permeability of materials, particularly those with specific porosity ranges, was estimated using tools such as Fiji and parametric regression[33].

DL models, including CNN and the Boltzmann method, showed potential in porosity estimations; however, they occasionally faltered with samples having low permeability[34]. Another approach, the C-Net model, was trained on 2D images to estimate porosity but had its limitations[35]. Similarly, a CNN-based computational framework had difficulties with materials of low diffusivity[36]. DL methods were also used for enhancing image resolution. 3D images were generated using generative adversarial neural networks (GAN), but the models often produced less accurate permeability values[37]. Techniques such as 3D multiscale imaging were applied to porous volcanic rock materials, but they sometimes overestimated porosity[38].

Recent studies have demonstrated the effectiveness of enhanced U-Net based segmentation models for pore structure and geomaterial analysis using micro-CT images[39]. DL based encoder decoder architectures have also been extensively evaluated for segmenting pore spaces and microfractures in digital rock images[40]. Unsupervised deep learning approaches have been explored to address the dependency on labeled datasets in micro-CT image segmentation, enabling reliable pore scale segmentation and contact angle estimation in multiphase CO_2 water rock systems without extensive manual annotation[41]. Advanced UNet++based workflows combined with energy-based modeling have further improved the segmentation of fine scale boundaries and small pore targets in digital rock images, highlighting the potential of DL methods to enhance porosity related feature extraction in heterogeneous geological materials[42].

Practical challenges with 2D CNN segmentation include limited training data and model flexibility. Although 3D CNN models yielded high-accuracy results, they were resource-intensive with scalability concerns[43]. Semi-automated techniques exhibited high accuracy, albeit with significant error rates[44]. CNN models such as SegNet and U-Net achieved commendable accuracy rates but produced inaccuracies with microporous materials[45,46]. A novel framework used CNN to estimate various properties of sandstones, highlighting the potential and current limitations of DL in digital rock analysis[47]. Table 1 summarizes the studies that used image segmentation and CNN models for analyzing material properties.

As a summary the material properties evaluated using traditional imaging methods, which were limited by their complexity are improved by machine learning techniques, notably DL. Models such as Inception and ResNet could estimate material properties, such as porosity and permeability, from X-ray μCT images. Efforts to convert 2D images into 3D demanded additional input information about the material samples. Pixel-wise classification has unveiled challenges such as training data availability and scalability. Artificial Intelligence is widely used for analyzing material properties and combining traditional and innovative computational methods is crucial. Using CNN, a stacked model is proposed herein to estimate material porosity from 2D CT images. A DeepCNN model was used for material classification and a rule-based adaptive threshold (RBAT) technique was developed for porosity estimation. The efficacy of the proposed method was validated by comparing the results with those obtained using the vacuum pycnometer (PYC) method[48].

Methodology

A robust methodology for estimating porosity from CT images of materials was provided, without the use of supplemental data. Figure 1 illustrates the proposed methodology, outlining each step in detail. The initial dataset consisted of 2D CT scans representing different classes of construction materials, specifically cement-based mortar (CM0, CM5, CM10, CM20), geopolymer-based mortar (Geo), and ultra-high-performance concrete (UHPC). The three materials display markedly divergent pore architectures, from the relatively open systems in conventional mortar to the packed, fine-scale pores in ultra-high-performance concrete (UHPC) and the chemically unique matrix of geopolymers. Assessing all three facilitates the evaluation of the model's resilience across a diverse range of pore shapes. The obtained 2D CT pictures inherently exhibit several imaging abnormalities, such as X-ray scattering, beam hardening effects related to the Beer–Lambert attenuation principle, moisture-induced scattering in cementitious materials, and edge effects stemming from specimen geometry. Edge effects and acquisition-related frame abnormalities induce non-representative intensity fluctuations around specimen borders, potentially resulting in erroneous porosity estimation if incorporated into the study. This study addresses the issue by explicitly separating the actual region of interest (ROI) before calculating porosity. A DeepCNN-based object detection framework is utilized to autonomously identify and extract the internal specimen region, while disregarding peripheral frame-like patterns and boundary areas influenced by edge artifacts. This automatic ROI extraction guarantees that porosity is calculated just from the

Refs.	Techniques	Input	Output	Experimental observations
[26]	Gradient boosting, SVM, and ANN	3D image of gas diffusion layers in fibrous materials	Diffusivity, permeability, and relative permeability	Gradient boosting attained a higher accuracy of ~ 95% in predicting the porosity of the trained materials. The accuracy significantly decreased in all models for unknown materials.
[32]	Nonlocal means (NLM) denoising, CNN, and quantitative analysis	3D X-ray tomographic images of low-density ceramics	3D image of input, pore density, and porosity	Denoising is substantive with low contrast images. Parameter estimation was longer with unfamiliar materials. Annotation and training of CNN models were time-consuming and captive to human bias.
[33]	ImageJ FIJI tool and computational fluid dynamics	3D X-ray tomography image of honeycomb materials	Porosity, median pores size, and permeability	Data from physical methods were used for determining the correlation between the porous parameters obtained from image processing. Permeability predictions were accurate only with the studied material.
[34]	CNN and lattice Boltzmann method	Binary images of multiple porous media and related variables obtained from simulations	Porosity, permeability, and tortuosity	Predicted porosity, permeability, and tortuosity with a relative error of 6% from true values. The model faced challenges in accurate prediction for low permeability and tortuosity of > 1.75. Moreover, reasonably accurate predictions were obtained only for the data they were trained on.
[35]	C-Net and U-Net with self-normalization module [23]	Binary images of multiple porous media with geometrical data	Porosity and effective diffusivity	Achieved improvement in prediction accuracy of porosity and diffusion coefficient with 1σ of confidence than their previous model [23].
[36]	CNN	2D binary images of porous materials	Porosity and effective diffusivity	The model had greater variation ranges (0.28–0.98) from the ground truth across diversified and complex structural topologies.
[37]	GAN and lattice Boltzmann method	2D TXM and FIB-SEM images of rock samples	Permeability and 3D image of the input	Computed permeability by reconstructing 3D volume image from the 2D image. The computational time of the model is greater and increases with structural complexity of the material.
[38]	2D U-Net and Pix2pix networks	3D μCT images of volcanic rocks with low, high, and very high resolutions	Porosity, permeability, and diffusivity	The model took a long time for dataset preparation. Porosity values were overestimated for low-resolution image samples.
[43]	2D and 3D configurations of SegNet, U-Net, ResNet, U-ResNet, and MultiResNet	μCT images of multimineral rock samples	Space and absolute permeability	Among all the models, the prediction accuracy of U-ResNet-3D was closer to the ground truth. However, the performance was inconsistent for some materials.
[28]	InceptionNet-v3, InceptionNet-v4, InceptionNet-slim, and ResNet	SEM images of multiple objects of different scales	Classification of pixels as pores and solid regions	Manual labeling of the dataset was time-consuming. Model performance was very low for images with divergent characteristics.
[29,30]	PiXelNet and Max-voted segmentation based fully connected CNN	SEM images of carbon steel microstructures	Classification of pixels as pores and solid regions	Models efficiently analyzed the physical features of massive known target materials.
[45], [46]	SegNet, extended SegNet, and U-Net	Tomographs of three homogeneous sandstones	3D image of the sampled material	Improved accuracy up to 99% using multiphase thresholding techniques.
[47]	CNN framework hybrid with Otsu, network extraction algorithm, watershed algorithm, and Gaussian filter	μCT images of sandstones	Porosity, specific surface area, and average pore size	CNN-predicted porosity showed a relative error of 2.7% on binary images whereas the error increased to 6.3% for grayscale images. The method is dependent on the thresholding techniques and suffers from uncertainty.

Table 1. Summary of related research.

center, physically representative area of the specimen, thus reducing the impact of boundary-induced mistakes. Pores that intersect the specimen margins or are influenced by geometric distortion are systematically omitted from porosity estimation. Material classification is crucial as each material type displays unique grayscale properties and pore differentiation. The RBAT module implements distinct thresholding criteria for each class, and precise classification guarantees the appropriate rule set is utilized, enhancing segmentation quality and porosity assessment.

Due to the susceptibility of manual ROI delineation to errors and the time-intensive nature of the process, an automated solution was proposed, wherein a specialized DeepCNN model was trained. This model was designed to inherently identify and extract the ROI from the input images, thereby eliminating manual intervention. For training, as the first step, the dataset was manually annotated by demarcating the boundaries around the ROIs and tagging them with their respective material classes. In the proposed methodology, precise annotation of input images is emphasized, including the identification of object corners and material classes, essential for accurately estimating porosity, even for partially visible pores. The DeepCNN model is trained with a dataset enriched by images featuring various pore visibility scenarios, enabling the precise detection of object boundaries and the inclusion of partially cropped pores in the porosity analysis. This approach ensures that porosity estimates accurately reflect material characteristics, even when the complete pore structure is not fully observable. Moreover, to enhance the model performance and counteract overfitting, data augmentation techniques were used. After isolating the ROI, as the next step the DeepCNN model further processed the image primarily for segmenting the ROI and classifying the underlying material type. The resultant output was a segmented ROI image, duly classified under one of the material classes.

The third step, the porosity was estimated by considering high-intensity pixels as pores and low-intensity pixels as the background. A clustering approach was used to distinguish these regions, and pixels were categorized based on their intensity. To further refine the clustering output, RBAT was used. It automatically derived a threshold value for any given image and converted the clustered image into a binary format, wherein pixels with intensity values of 255 and 0 are interpreted as pores and background, respectively. Finally, porosity was quantified by calculating the ratio of pixels classified as pores to the total number of pixels within the cropped ROI and the result was expressed as a percentage. This approach ensures that porosity estimation is not influenced by non-sample

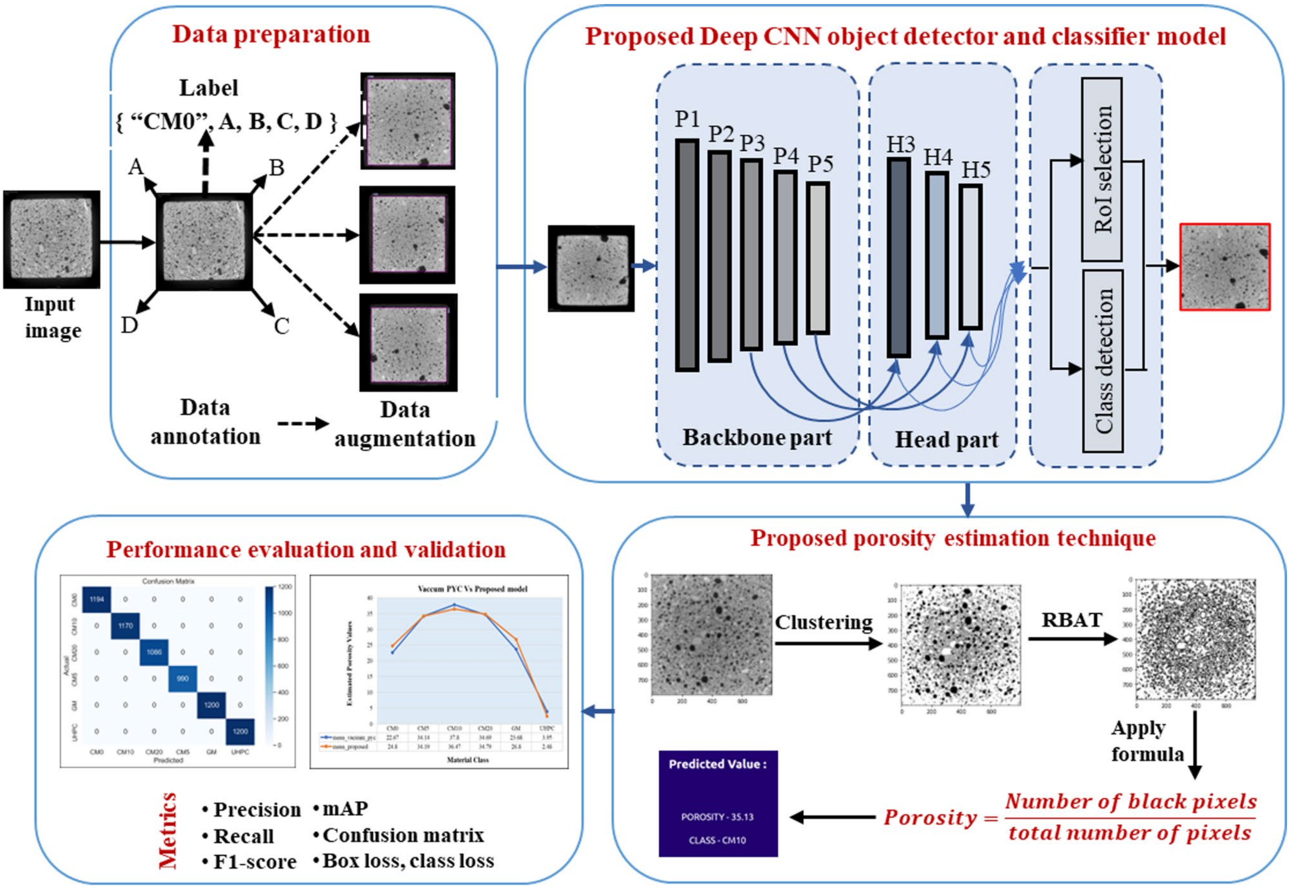

Fig. 1. Workflow of the proposed method.

regions or boundary-related artifacts present in the original CT images. For validation, the porosity estimated using the proposed model was compared with the ground truth values obtained using the conventional vacuum PYC method. The DeepCNN model is used exclusively for material classification and automated extraction of the region of interest from the micro-CT images. Although internal feature maps are generated during the network's forward pass, these are not used to produce pore-level segmentation masks. All pore segmentation is performed in a subsequent stage using the rule-based adaptive thresholding approach. This separation ensures a clear distinction between learning-based classification and rule-based porosity segmentation.

DeepCNN architecture for material classification

DeepCNN, an advanced architecture, is used for object detection, particularly for distinguishing various materials based on their inherent patterns and textures. The DeepCNN architecture follows the design principles of single stage object detection frameworks, particularly YOLO based models that combine convolutional backbones, spatial pyramid pooling, and prediction heads for region localization and classification[49]. In this work, the YOLO style architecture is adapted and simplified for material specific ROI detection in CT images, with the feature fusion neck omitted to reduce computational complexity and support efficient porosity estimation[50]. The architectural framework of DeepCNN is structured around three core components as illustrated in Fig. 2. First, CNN acts as the architectural backbone for extracting intricate features from the input images. Second, an intermediary "neck" network (SPPNet) composed of convolutional and pooling layers refines the features obtained from the backbone and optimizes them for object detection tasks. Lastly, the "head" network, another specialized CNN, classifies potential object regions and meticulously calibrates their spatial coordinates.

Sample Preparation and imaging

The Portland cement-based mortar specimens (CM0 - CM20 series) were prepared using a water to cement ratio of 0.45, while the ultra-high performance concrete specimens were produced with a water to binder ratio of 0.20. All Portland cement based and UHPC samples were cured under controlled laboratory conditions and scanned at an age of 28 days. This curing duration ensured hydration stability prior to imaging and minimized moisture related variability in X ray attenuation. The geopolymer specimens were cured at elevated temperature for the initial 24 h and subsequently stored under ambient laboratory conditions before scanning. This preparation and curing conditions were selected to ensure a consistent internal moisture distribution across samples and to reduce its influence on grayscale contrast during micro-CT image reconstruction.

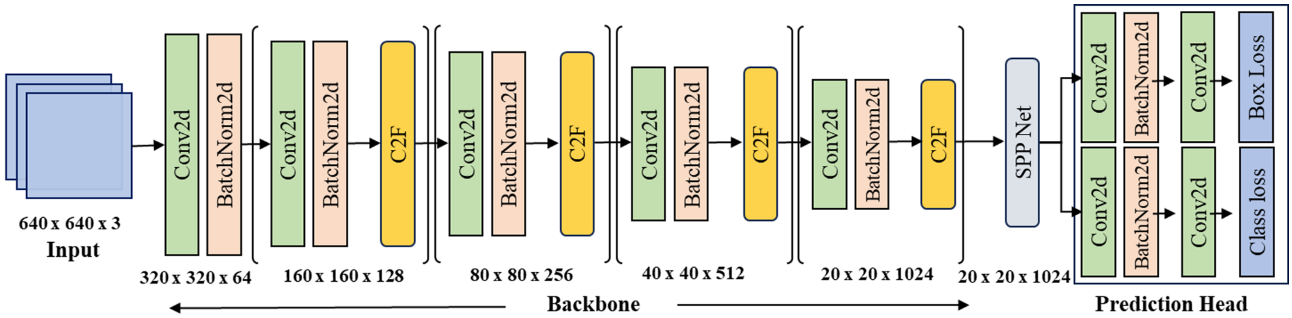

Fig. 2. DeepCNN architecture for object detection.

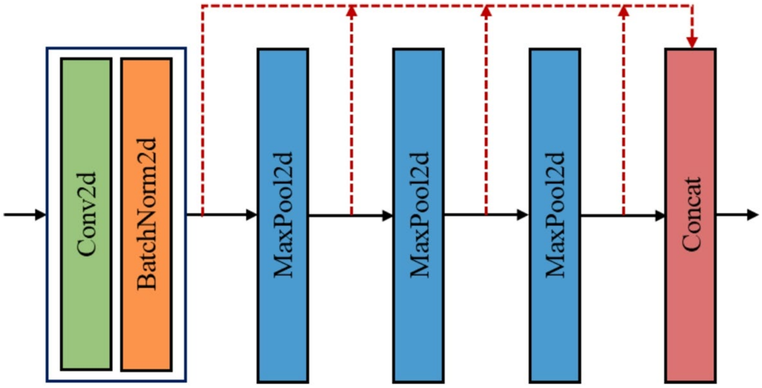

Fig. 3. SPPNet architecture for object detection.

All specimens were scanned using a laboratory X ray micro computed tomography system operated at an accelerating voltage of 90 kV. A beam hardening filter was applied to reduce reconstruction artifacts. Projection images were acquired over a full rotation and normalized using open and closed beam reference images prior to reconstruction. The reconstructed volumes provided a voxel resolution of approximately 2 µm, which was sufficient for subsequent pore segmentation and porosity estimation.

During the training phase, the model used a composite loss function, integrating both classification and regression losses. First, the model was trained to demarcate potential object regions. Then, its ability was improved to accurately classify these regions and refine their boundaries. During operation, the model used the SPPNet network after feature extraction for preliminarily predicting the object region and the prediction head network for final classification and boundary precision, ensuring the accurate detection and localization of objects within the images.

Spatial pyramid pooling network (SPPNet) plays a vital role in object detection models by enhancing their adaptability to variations in the size and scale of input images. The SPPNet layer partitions the extracted features into a grid format as shown in Fig. 3. Within each grid cell, it applies a max pooling operation to distill the most significant information. The outcomes of these pooling processes are then merged to form a consistent-sized vector. This resultant vector is fed into the fully connected layers of the model for object identification and accurate prediction of their boundaries. SPPNet is especially beneficial in two-phase object detection models. In the first phase, potential object locations are determined; in the second phase, these predictions are further refined. Using SPPNet, these models exhibit improved accuracy for varied datasets. SPPNet also prevents overfitting by reducing the model's dependence on the specific arrangement of features in the input image. The following algorithm explains the working of DeepCNN for feature extraction and classification of materials.

Porosity estimation

Portland cement-based materials exhibit a multi-scale pore system comprising entrained and entrapped air voids, shrinkage-induced pores, capillary pores, and gel pores. Due to resolution limitations, micro-computed tomography imaging captures only pores larger than the effective voxel size, primarily representing entrained, entrapped, and large capillary pores. In contrast, vacuum pycnometer measurements account for the total accessible pore volume, including sub-resolution gel and fine capillary pores. The agreement observed between the two methods in this study should therefore be interpreted at a comparative, material-class level rather than as a direct equivalence of absolute pore volumes. Within a given mixture type, the fraction of sub-resolution pores is expected to remain relatively consistent across specimens, allowing trends in porosity variation to be meaningfully compared. As a result, although the absolute pore-size ranges differ, the micro-CT–based estimates

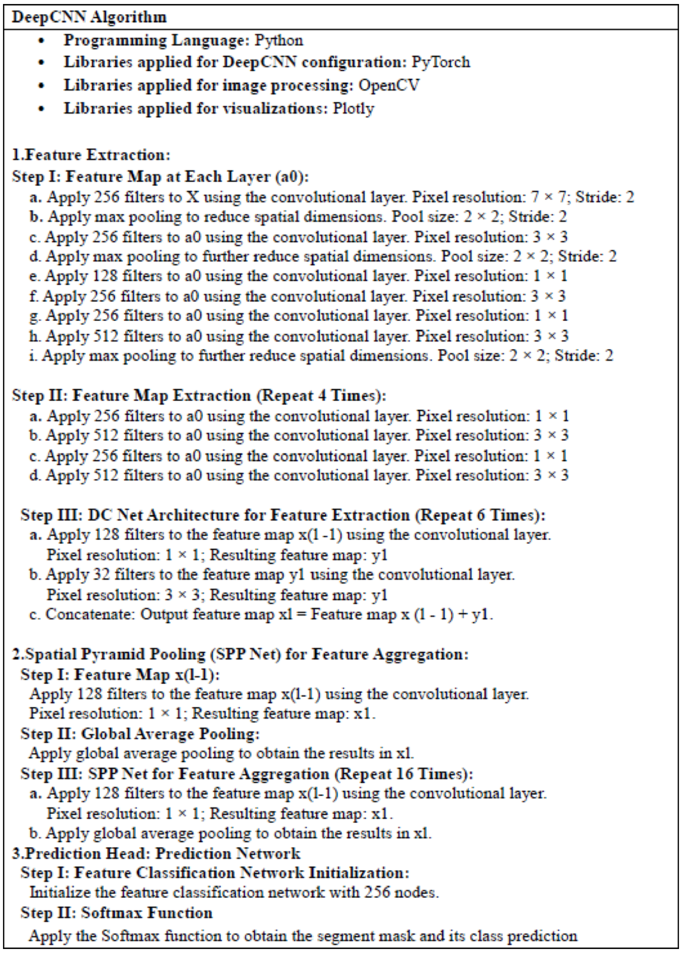

```
DeepCNN Algorithm
  • Programming Language: Python
  • Libraries applied for DeepCNN configuration: PyTorch
  • Libraries applied for image processing: OpenCV
  • Libraries applied for visualizations: Plotly

1.Feature Extraction:
Step I: Feature Map at Each Layer (a0):
  a. Apply 256 filters to X using the convolutional layer. Pixel resolution: 7 × 7; Stride: 2
  b. Apply max pooling to reduce spatial dimensions. Pool size: 2 × 2; Stride: 2
  c. Apply 256 filters to a0 using the convolutional layer. Pixel resolution: 3 × 3
  d. Apply max pooling to further reduce spatial dimensions. Pool size: 2 × 2; Stride: 2
  e. Apply 128 filters to a0 using the convolutional layer. Pixel resolution: 1 × 1
  f. Apply 256 filters to a0 using the convolutional layer. Pixel resolution: 3 × 3
  g. Apply 256 filters to a0 using the convolutional layer. Pixel resolution: 1 × 1
  h. Apply 512 filters to a0 using the convolutional layer. Pixel resolution: 3 × 3
  i. Apply max pooling to further reduce spatial dimensions. Pool size: 2 × 2; Stride: 2

Step II: Feature Map Extraction (Repeat 4 Times):
  a. Apply 256 filters to a0 using the convolutional layer. Pixel resolution: 1 × 1
  b. Apply 512 filters to a0 using the convolutional layer. Pixel resolution: 3 × 3
  c. Apply 256 filters to a0 using the convolutional layer. Pixel resolution: 1 × 1
  d. Apply 512 filters to a0 using the convolutional layer. Pixel resolution: 3 × 3

 Step III: DC Net Architecture for Feature Extraction (Repeat 6 Times):
  a. Apply 128 filters to the feature map x(1 -1) using the convolutional layer.
     Pixel resolution: 1 × 1; Resulting feature map: y1
  b. Apply 32 filters to the feature map y1 using the convolutional layer.
     Pixel resolution: 3 × 3; Resulting feature map: y1
  c. Concatenate: Output feature map xl = Feature map x (1 - 1) + y1.

2.Spatial Pyramid Pooling (SPP Net) for Feature Aggregation:
 Step I: Feature Map x(l-1):
  Apply 128 filters to the feature map x(l-1) using the convolutional layer.
  Pixel resolution: 1 × 1; Resulting feature map: x1.
 Step II: Global Average Pooling:
  Apply global average pooling to obtain the results in xl.
 Step III: SPP Net for Feature Aggregation (Repeat 16 Times):
  a. Apply 128 filters to the feature map x(l-1) using the convolutional layer.
     Pixel resolution: 1 × 1; Resulting feature map: x1.
  b. Apply global average pooling to obtain the results in xl.
3.Prediction Head: Prediction Network
 Step I: Feature Classification Network Initialization:
  Initialize the feature classification network with 256 nodes.
 Step II: Softmax Function
  Apply the Softmax function to obtain the segment mask and its class prediction
```

reflect relative porosity differences that align with experimental measurements obtained using the vacuum pycnometer.

Clustering

A CT scan of the specimen utilized in this study had several color spaces. One of the most significant issues was figuring out which layers was on top and which have been on the bottom in the image. This is important for telling the difference between the real pores and solid areas of the specimen. K-means clustering is employed for intensity-based separation of pore and solid regions, following its extensive and validated use in image segmentation and pattern analysis reported in high impact computer vision and image analysis journals[51]. The image pixels are sorted by their color spaces and used K-means clustering to group them because it works well for grouping pixels. Prior to thresholding, K-means clustering was applied to the grayscale image to group pixels with similar intensity values. Each image was reshaped into a one-dimensional pixel array and normalized to reduce intensity variations. The clustering was performed using three clusters, representing pore regions, solid matrix, and transitional grayscale values. This step provides a stable pre-segmentation that reduces sensitivity to noise and improves the robustness of subsequent thresholding operations.

Figure 4 depicts the steps involved in clustering. As the first step, the image was vectorized before clustering for subsequent detailed analysis. Then, K-means clustering determines the optimal cluster count, which is denoted as "k." Several trials were conducted by assigning different values for k, herein to determine the optimal k. The estimated porosity obtained using k was compared with the observed porosity of the specimen. For $k = 3$, the estimated and observed porosity values agreed well with high fidelity. Thus, the proposed method suggests that $k = 3$ is ideal because the image pixel values were adeptly allocated to their nearest clusters.

RBAT

After the images were clustered and cropped, adaptive thresholds were applied to differentiate various classes, resulting in a binary representation of the material. For "CM0" materials, image processing was performed by first applying a median blur filter (kernel size of 5) to mitigate image noise. Then, mean adaptive thresholding was applied for determining a threshold for each pixel based on the mean intensity of its surrounding area, facilitating effective segmentation. Adaptive threshold selection follows Otsu based histogram thresholding principles, and the associated clustering and thresholding operations are implemented using OpenCV based image processing routines that are widely adopted and validated in scientific image analysis workflows[52,53]. Such preprocessing is vital for accurate porosity estimation of CM0 materials, ensuring noise-free images and highlighting relevant features.

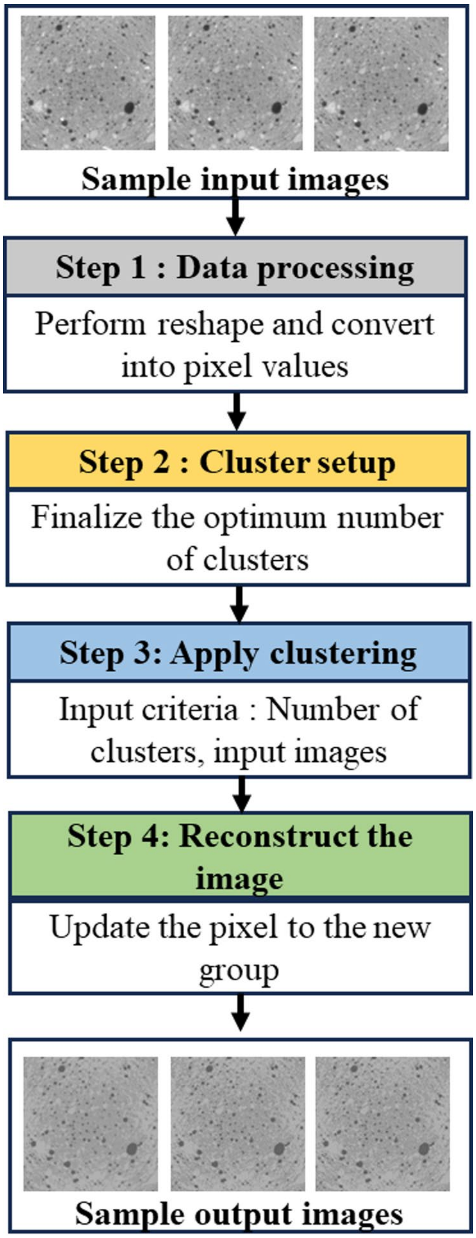

Fig. 4. Clustering process.

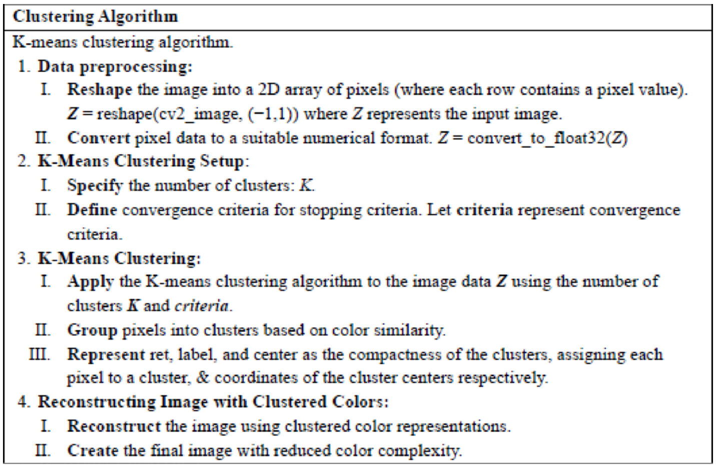

```
Clustering Algorithm
K-means clustering algorithm.
1. Data preprocessing:
    I.   Reshape the image into a 2D array of pixels (where each row contains a pixel value).
         Z = reshape(cv2_image, (−1,1)) where Z represents the input image.
    II.  Convert pixel data to a suitable numerical format. Z = convert_to_float32(Z)
2. K-Means Clustering Setup:
    I.   Specify the number of clusters: K.
    II.  Define convergence criteria for stopping criteria. Let criteria represent convergence
         criteria.
3. K-Means Clustering:
    I.   Apply the K-means clustering algorithm to the image data Z using the number of
         clusters K and criteria.
    II.  Group pixels into clusters based on color similarity.
    III. Represent ret, label, and center as the compactness of the clusters, assigning each
         pixel to a cluster, & coordinates of the cluster centers respectively.
4. Reconstructing Image with Clustered Colors:
    I.   Reconstruct the image using clustered color representations.
    II.  Create the final image with reduced color complexity.
```

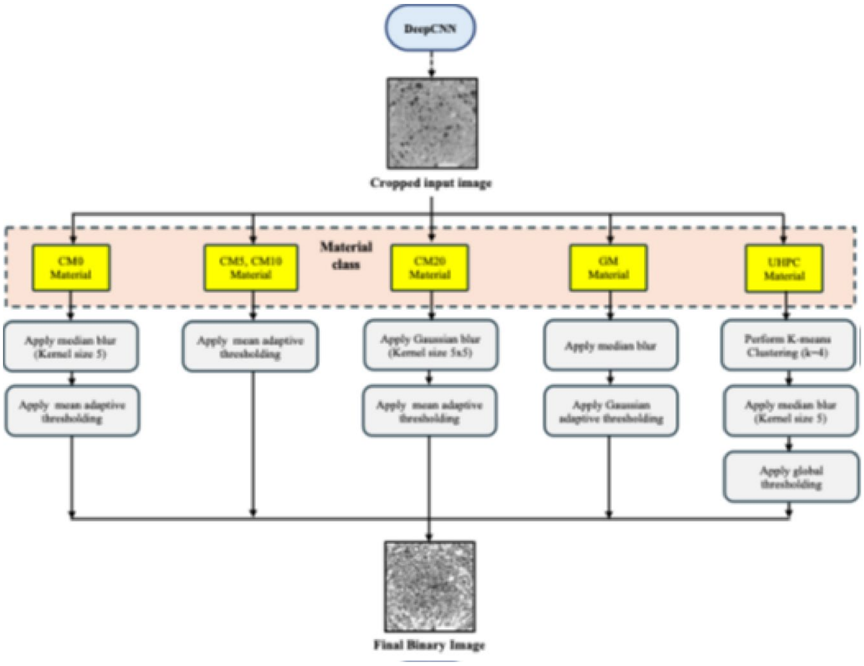

Fig. 5. Overview of the RBAT workflow.

The rule-based adaptive thresholding module dynamically selects an appropriate thresholding strategy based on the grayscale distribution and noise characteristics of the classified material. For materials with high contrast and low noise, a global threshold is applied. In cases where intensity variation is higher, adaptive mean or Gaussian thresholding is employed. The decision logic is guided by material classification results and clustering statistics. Figure 5 represents the schematic overview of the RBAT workflow, illustrating the decision pathway from input image to final binary pore segmentation.

For "CM10" or "CM5" materials, the segmentation process was streamlined, and mean adaptive thresholding was applied without prior blurring to the gray-scale image. This process is suitable for materials with minimal noise or wherein maintaining fine structural details in image is essential for porosity estimation. For "CM20" materials, a Gaussian blur filter (kernel size of 5 × 5) was first applied to smooth the image and reduce noise, followed by mean adaptive thresholding. The Gaussian blur ensured the image remained largely unaffected by noise, and the subsequent thresholding segmented relevant regions. This combination is well-suited for images of CM20 materials with moderate noise levels.

A procedure similar to that for "CM0" materials for used for "GM" materials but with a different method to adaptive thresholding. A median blur was first applied to the image for noise reduction, and adaptive thresholding using the Gaussian method was applied. This method is particularly effective for images with varying lighting conditions. The Gaussian method assigned varied weights to neighboring pixels, accommodating local intensity variations. Lastly, for "UHPC" materials, the image underwent K-means clustering with K = 4, segmenting it based on color or intensity similarities. The clustered image was then converted to grayscale for simplification. A median blur was applied to mitigate noise, followed by global thresholding. This comprehensive approach is tailored for UHPC materials, allowing precise segmentation and accurate porosity estimation by differentiating material components within the image.

Porosity estimation

Binary images of the materials were obtained for porosity estimation using a rule-based approach. These images were representative of the material samples, with pixel values typically indicating either the material structure (0) or the pores (255). This method was primarily used for quantifying the void or pore space within a material, which is crucial for material characterization. First, the binary image was converted into a vector array for data manipulation. Then, distinct pixel values in the binary image representing the material structure (denoted by 0) and pores (denoted by 255) were identified.

Porosity was calculated using a mathematical formula shown in Eq. 1 that computes the ratio of the pore pixel count to the total pixel count in the image for pores and solid structure.

$$\text{Porosity} = \frac{\text{Pixel values of the pores}}{\text{Total EquationNumber of pixels}} \times 100 \tag{1}$$

	Dataset description			Data split	
Material class	Collected images	Augmented images	Total images	Training phase	Testing phase
CM0	1201	2402	3603	2882	721
CM5	989	1978	2967	2374	593
CM10	1169	2338	3507	2806	701
CM20	1081	2162	3243	2594	649
GM	1200	2400	3600	2880	720
UHPC	1200	2400	3600	2880	720
Total	**6840**	**13,680**	**20,520**	**16,416**	**4104**

Table 2. Dataset description.

Experiment and results

Data Preparation

A dataset containing CT scans of various materials such as Portland cement type I (used for CM and UHPC), metakaolin (for GM), and silica fume (used as a pozzolanic additive in both UHPC and GM) was used. An alkali-activating solution containing sodium hydroxide was prepared for the geopolymer. In UHPC, silica flour and sand were incorporated as aggregates. Aluminum powder acted as an air-entraining agent for the foamed CM samples. CT measurements were performed to analyze specimens measuring 50 × 50 mm[244]. High – resolution CT scan images of materials having intricate structures at micro and even nanoscales produce vast amounts of data. The storage, management, and processing of these extensive datasets demand substantial computational capabilities. The processing and reconstruction of CT-scan data, particularly at higher resolutions, are resource-intensive and expensive. When trained with limited amounts of data, the DL models are prone to overfitting. To address this challenge, the dataset was augmented herein using image enhancement techniques, such as rotation, cropping, and flipping.

Herein, 2D CT scans that featured a black frame-like border, encompassing approximately 15% of the image periphery, were used. The proposed workflow was structured into two primary segments: material detection and classification as well as porosity estimation. Initially, images in the dataset were annotated with their respective class labels, accompanied by bounding box coordinates highlighting the material's ROI. Directly using the images from the CT-scan device led to erroneous porosity values, as the black border was inadvertently included in the estimation. Thus, the DL model was used to identify and isolate the ROI, thereby effectively removing the extraneous black frame. This DL model was trained using class labels such as CM0, CM5, CM10, CM20, GM, and UHPC. Table 2 shows the distribution of data for both the testing and training phases.

Performance evaluation

The performance of the proposed deep learning (DL) model in material classification and porosity estimation is comprehensively assessed using key evaluation metrics, including box loss, class loss, mean average precision (mAP), and intersection over union (IoU) at specific thresholds. These metrics facilitate a nuanced understanding of the model's effectiveness and accuracy across various dimensions. Box loss evaluates the precision in identifying the boundaries of objects or regions of interest (ROIs) within images, with a lower score indicating a closer match between the model's predictions and actual object boundaries. Class loss, on the other hand, quantifies the model's ability to correctly classify the materials depicted in the images, with lower values signifying higher classification accuracy.

Furthermore, the model's performance is also gauged through mean average precision (mAP), which provides an overarching score for the precision of object detection across different classes and IoU thresholds, and intersection over union (IoU), which measures the overlap between predicted and actual bounding boxes. An IoU of 1 represents a perfect overlap, indicating highly accurate object localization. The DL model's loss at each iteration reflects a blend of coordinate and classification losses, where coordinate loss is determined by the degree of overlap between actual and predicted bounding boxes, and classification accuracy is illustrated through a confusion matrix that includes precision and recall metrics.

Collectively, these metrics provide a detailed assessment of the DL model's capability to accurately locate and classify objects within images, which is pivotal for accurately determining the material's ROI for porosity computation and enhancing the model's utility in practical applications.

Model performance on material classification

The performance of the DL model was evaluated during the training and testing phases. The model was trained for 20 iterations with a batch size of 10. Figure 6 shows the learning performance of the model during classification. As the number of epochs increases, the model's error rate consistently decreases, showcasing a significant improvement in its predictive accuracy and demonstrating its capacity to effectively learn from the training data. This trend not only signifies the model's adeptness at adapting to the underlying patterns within the data but also highlights the implementation of comprehensive measures designed to ensure its robustness and general applicability. To prevent overfitting and maintain the model's performance across various datasets, strategies such as regularization, early stopping, and data augmentation have been meticulously employed, thereby enhancing the model's ability to generalize to unseen data. Figure 6(a) shows the box loss of the model during the training and cross-validation phases. In Fig. 6(b), the plot for IoU at the thresholds of 0.5 and 0.5–

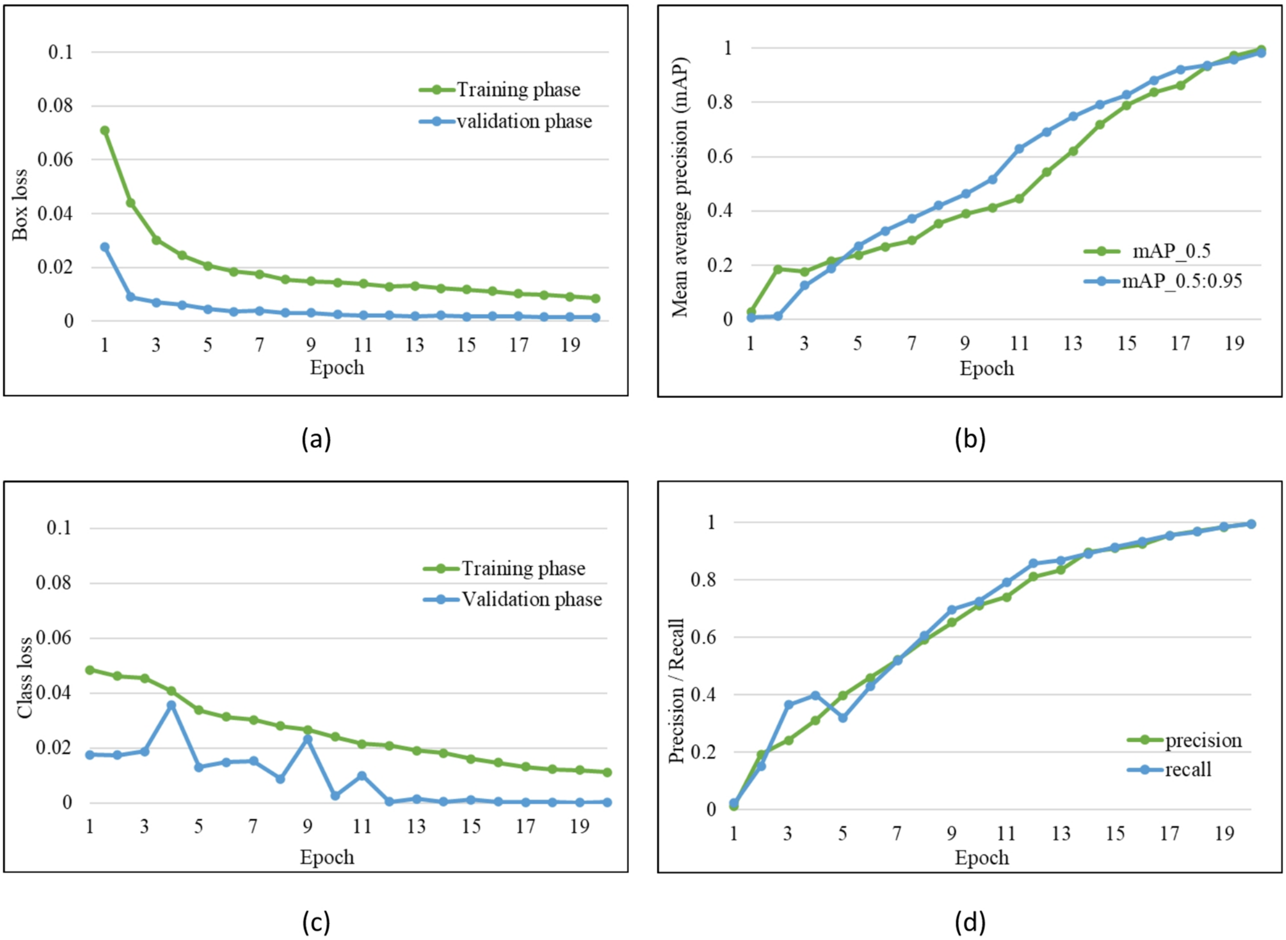

Fig. 6. DeepCNN model performance during the learning phase. (**a**) Box loss; (**b**) IoU with mAP threshold of 0.5 and 0.5–0.95; (**c**) class loss; and (**d**) precision versus recall.

0.9 mAP demonstrates a consistently improving performance, with more accurate bounding boxes around the ROI over successive epochs. Figure 6(c) shows that the model's class loss remained steady during training but exhibited some variability during the validation phase. Figure 6(d) indicates a positive trend in learning, with both precision and recall values showing consistent growth during both phases.

The model performance was assessed using a specific image set; the results are shown in Fig. 6. The dataset used herein was imbalanced. Precision–recall (PR) plots are particularly valuable for gauging model performance for imbalanced datasets. Figure 7(a) shows that the model achieved an impeccable PR curve, with an area-under-curve value of 1 for all classes. Compared to the PR curve for the training phase, that for the testing phase exhibited a notable improvement. Figures 7(b) and 7(c) depict the variations in precision and recall with varying confidence threshold. As precision and recall increase, the confidence threshold for all classes also increases until the optimal value of 1. Figure 7(d) shows the plot of combined precision and recall values as a singular metric and F1-score against confidence threshold. A pronounced peak suggests an optimal balance between precision and confidence.

Figure 8 shows the confusion matrix used for evaluating the classification performance of the DL model. The proposed model was designed for multiclassification; therefore, the confusion matrix is plotted as 6 × 6 denoting the six classes of materials. Rows denote actual classes, and columns denote predicted classes. Diagonal elements represent correct classifications, whereas off-diagonal elements signify misclassifications. The confusion matrix results suggest that the model efficiently classifies all images.

Performance on porosity prediction

After material selection and classification, the porosity was estimated using the RBAT algorithm. The provided dataset contained the average porosity data for image samples from each class, as determined using the vacuum PYC method[44]. Porosity values for all images in the dataset were estimated, and an average value for each class was derived. The statistical distribution of the estimated porosity values using RBAT algorithm for 6,840 CT-scan images categorized under each class for 25%, 50%, and 70% of the dataset is presented in Table 3. This table clearly shows that the average porosity estimation remained consistent across each quartile of images for every class.

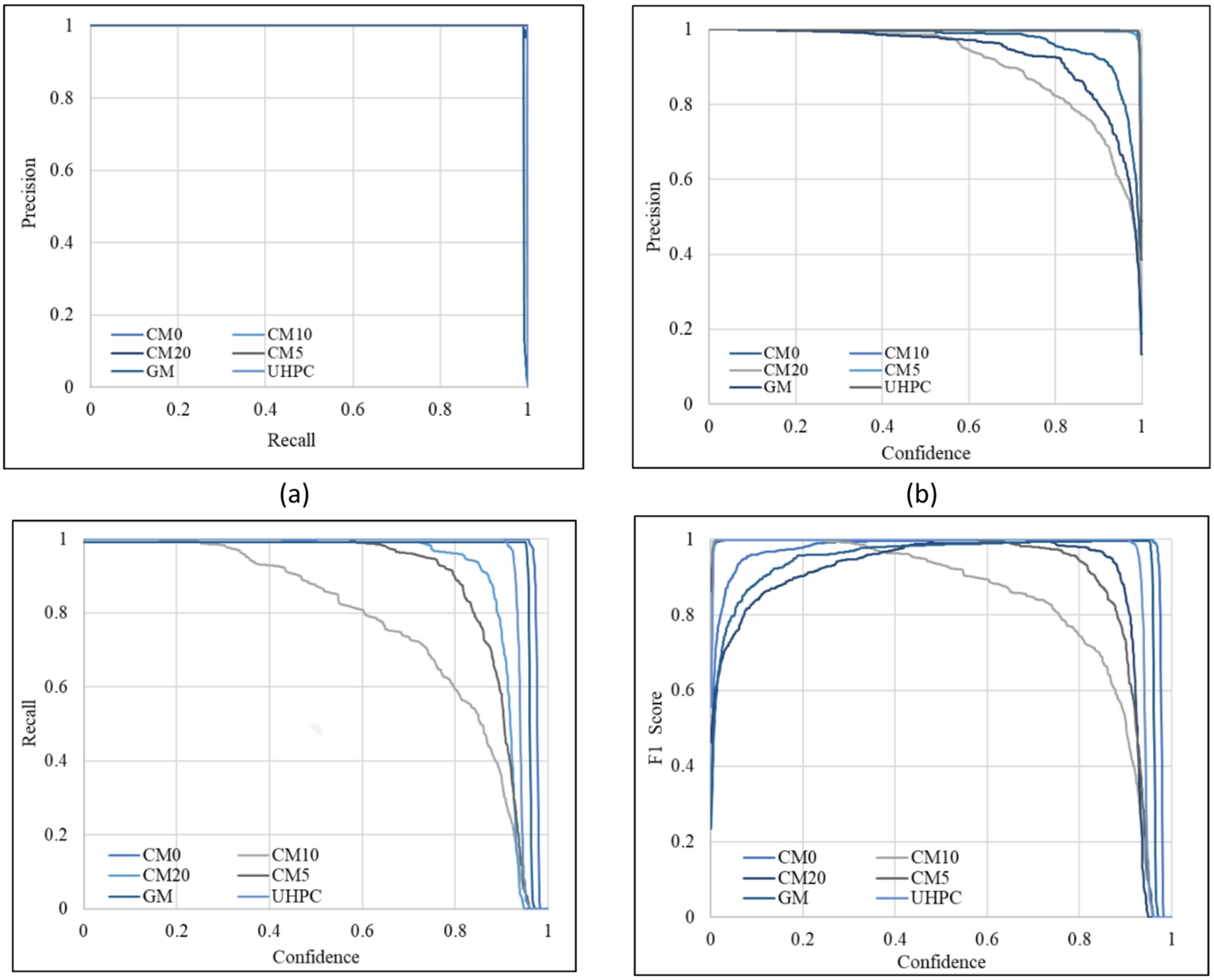

(a)

(b)

(c)

(d)

Fig. 7. Model performance during testing. (**a**) Precision versus recall; (**b**) precision versus confidence; (**c**) recall versus confidence; and (**d**) F1-score versus confidence.

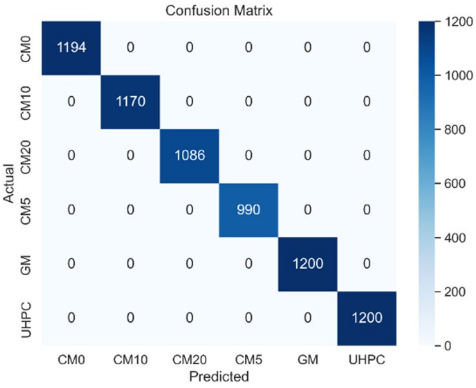

	CM0	CM10	CM20	CM5	GM	UHPC
CM0	1194	0	0	0	0	0
CM10	0	1170	0	0	0	0
CM20	0	0	1086	0	0	0
CM5	0	0	0	990	0	0
GM	0	0	0	0	1200	0
UHPC	0	0	0	0	0	1200

Fig. 8. Confusion matrix.

Figure 9 shows the distribution of the estimated porosity values for all images across each class within the dataset. The porosity distribution for CM0 (Fig. 9(a)) exhibits a relatively narrow spread around the mean, indicating uniform pore characteristics in the baseline material. A slight shift in mean porosity with increased dispersion is observed for CM5 (Fig. 9(b)), while CM10 (Fig. 9(c)) shows higher variability, reflecting progressive changes in pore structure with material modification.

Actual class	Image count	Average porosity	Min	Max	25%	50%	75%
CM0	1194	23.45	18.9	25.6	23.95	24.78	25.32
CM5	990	34.19	28.93	38.11	33.29	34.24	35.22
CM10	1170	36.47	34.04	38.25	36.15	36.55	36.86
CM20	1086	34.79	32.97	36.51	34.26	34.82	35.3
GM	1200	25.8	22.7	28.6	26.19	27.1	29.74
UHPC	1200	2.48	1.78	3.9	1.83	1.92	2.45

Table 3. Distribution of estimated porosity for different material classes.

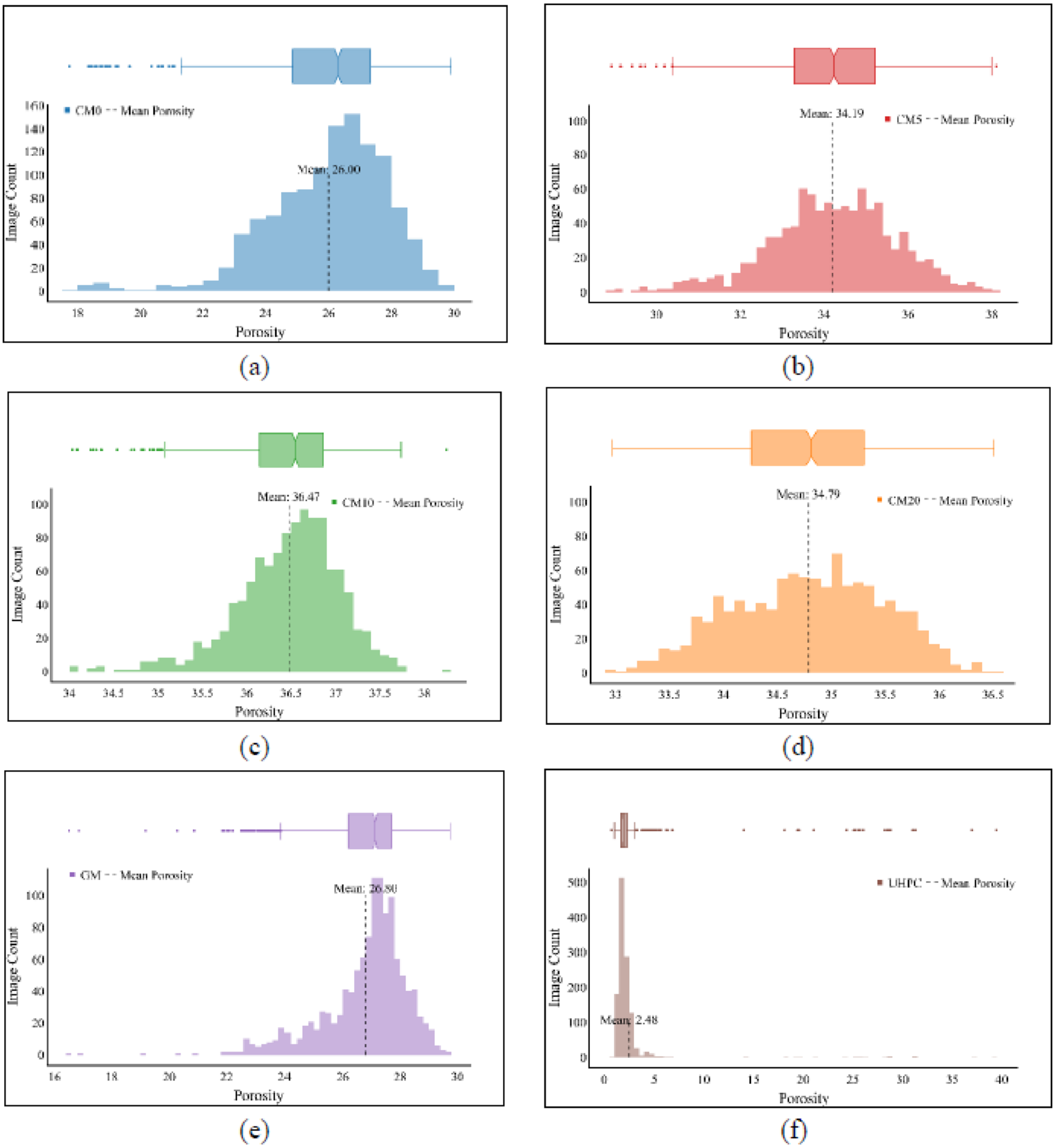

Fig. 9. Distribution of the estimated porosity for each material class (**a**) CM0; (**b**) CM5; (**c**) CM10; (**d**) CM20; (**e**) GM; and (**f**) UHPC.

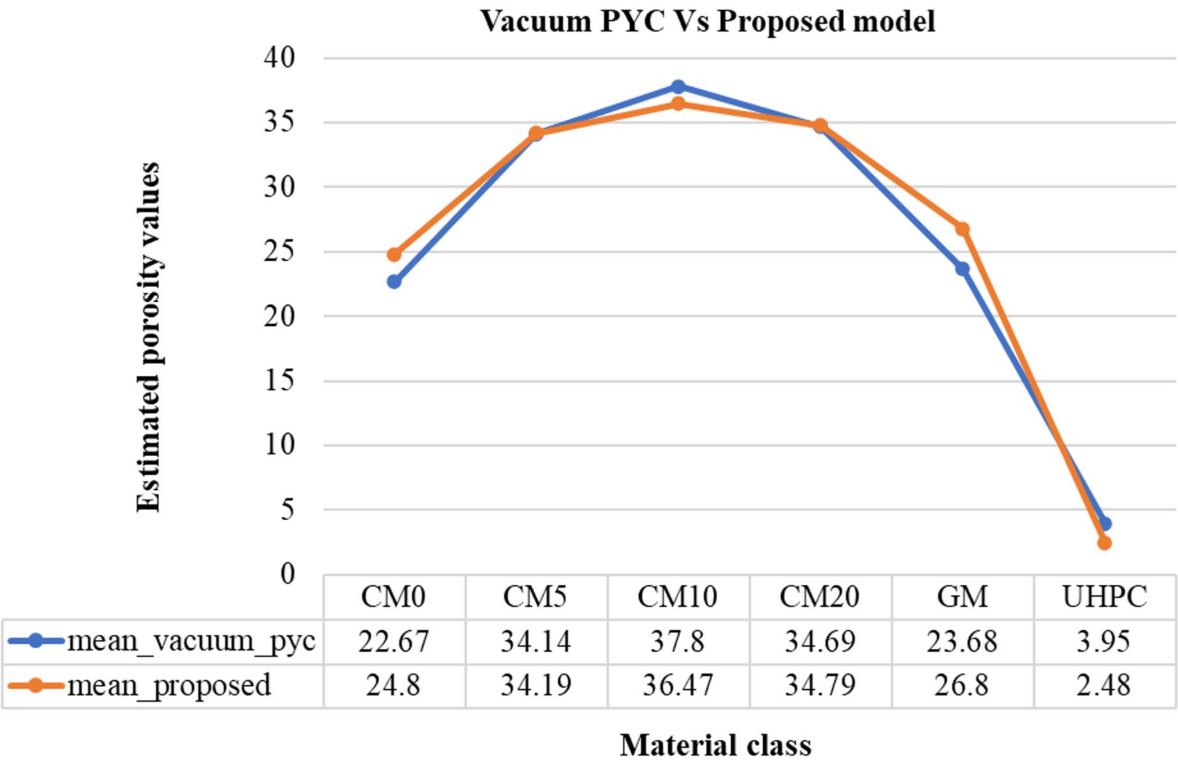

Fig. 10. Performance comparison of the proposed model with vacuum PYC method.

This distribution further reveals that some images have estimated porosity values that do not align with the typical range for their material class. Specifically, the distribution graph for class CM20 (Fig. 9(d)) exhibits no outliers, whereas GM (Fig. 9(e)) contains a small number of outliers, indicating moderate variability in pore distribution. Notably, UHPC displays a higher number of outliers compared to other classes, as shown in Fig. 9(f). These findings suggest that the model is particularly well fitted for CM20 but less fitted for UHPC, which exhibits a sparser pore distribution.

Performance comparison

The model's accuracy was validated by contrasting the results from the proposed method with those from the experimental vacuum PYC method[48]. Figure 10 displays a comparison chart, highlighting the mean values obtained from both methods across various material classes.

For CM0, the vacuum PYC method yielded an average porosity of 22.67, slightly lower than that estimated using the proposed method (24.8). For CM5, both methods yielded nearly identical values.CM10 showed a slight variation, with the porosity estimated by the vacuum PYC method (37.8) slightly higher than that estimated by the proposed method (36.47). The results obtained using both methods for CM20 results were almost similar (34.69 and 34.79 for the vacuum PYC and proposed method, respectively). The estimated porosity values were significantly different for GM, with 23.68 and 26.8 for the vacuum PYC and proposed method, respectively. Similar results were observed for UHPC: 3.95 and 2.48 for the vacuum PYC and proposed method, respectively. Overall, while both methods produced comparable results across most classes, the variability in the estimated porosity values for UHPC was particularly notable. The predicted porosity showed strong agreement with PYC results, with $R^2 = 0.96$ across all material classes and an average absolute percentage error below 3.2%. The RMSE values for CM-based materials ranged from 0.45 to 0.79.

Figure 11 illustrates the various transformations of the input image at every step of the proposed methodology and the predicted output, the material class along with the estimated porosity values of the input material image. The developed DeepCNN model identified the material class by leveraging the training data and used a logical formula (Eq. 1) to estimate the porosity based on the results from the RBAT module. The proposed method was effective in recognizing material classes, particularly for high-resolution images. However, the model encountered errors when processing low-resolution or noisy images.

Limitations and scope for future work

The suggested porosity estimation framework exhibits dependable performance for high resolution micro computed tomography images with distinct pore matrix contrast. However, several limitations must be addressed. The existing pipeline shows sensitivity to low resolution and noisy scans and relies on accurate material classification prior to RBAT. Since rule based adaptive thresholding predominantly depends on grayscale intensity differentiation, variations in image quality, noise, and contrast can compromise segmentation precision. In materials with highly heterogeneous pore distributions or minimal intensity contrast between pore

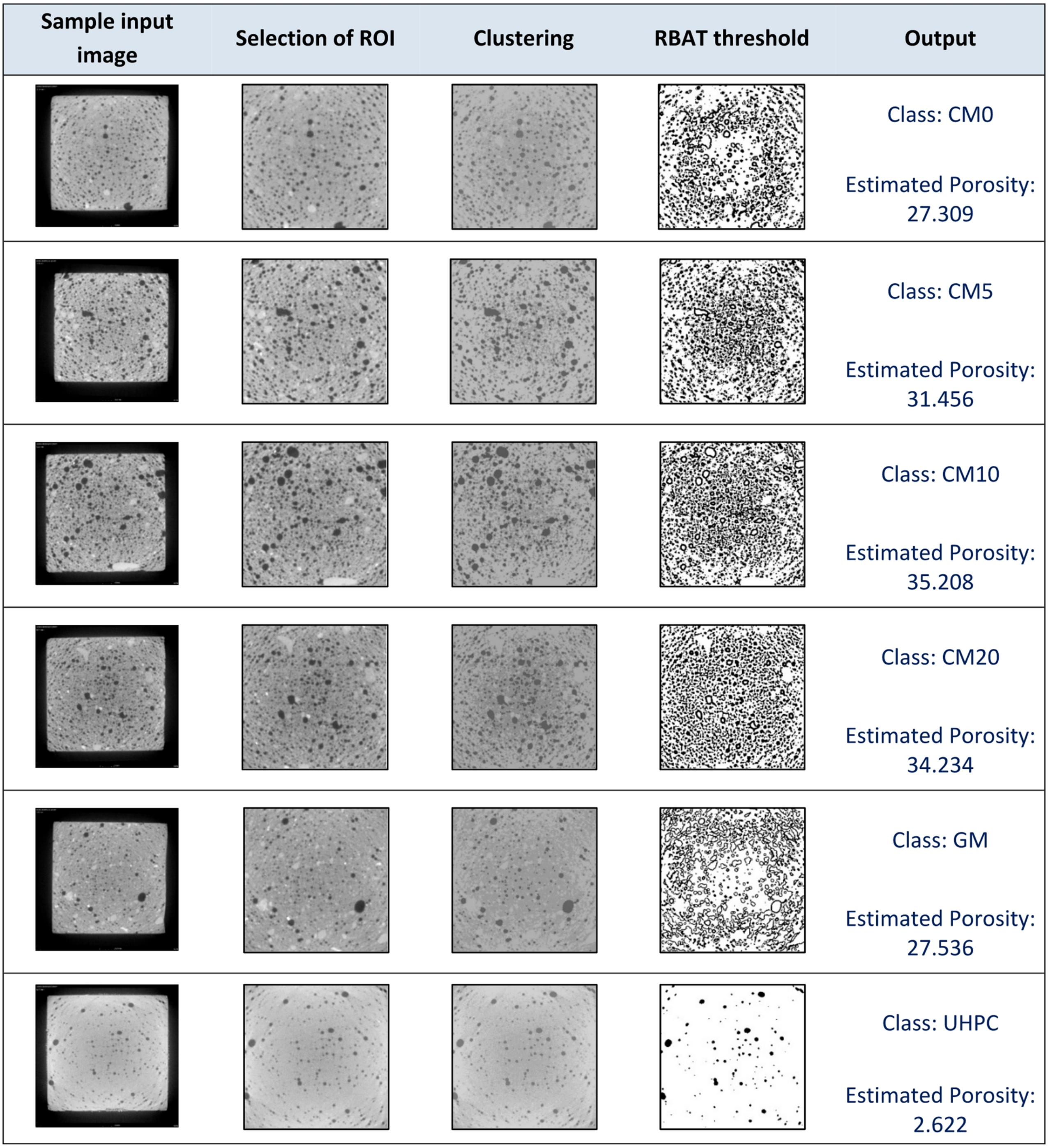

Fig. 11. Real-time experimental results.

and solid phases, partial pore misclassification may occur. The approach is further restricted to pores that are resolvable at the specified scanning resolution. Sub resolution pores, such as gel and capillary pores prevalent in cement based materials, cannot be explicitly segmented and are only indirectly reflected in the estimated porosity. This limitation is intrinsic to CT based imaging and affects all image driven porosity assessment methods. Reduced performance was also observed for material classes not included in the training set, indicating limited generalization to previously unseen material systems.

Recent studies have shown that semantic segmentation with data augmentation can improve pore segmentation in heterogeneous cementitious and composite materials[54]. Accordingly, future work will focus on enhancing the robustness and generalizability of the proposed framework by investigating learning based semantic segmentation approaches, including U Net and transformer based models, to address the limitations of threshold based segmentation in low contrast and complex imaging conditions[55]. To further mitigate sensitivity to low quality scans, denoising and contrast adaptive preprocessing techniques will be explored to improve feature consistency across diverse imaging settings. In addition, transfer learning and domain adaptation strategies will be examined to extend the applicability of the framework to novel cementitious and composite material systems. These developments are expected to improve segmentation accuracy, stability, and generalization across a wide range of material types.

Conclusion

Porosity is a critical parameter governing the mechanical, thermal, and chemical behavior of materials, yet its accurate estimation remains challenging due to limitations associated with manual intervention, imaging resolution, and conventional threshold-based techniques. In this work, a novel automated framework integrating DeepCNN based material classification with rule based adaptive thresholding has been proposed for porosity estimation from micro computed tomography images. The proposed model demonstrates computational efficiency, processing a μCT image in approximately 0.18 s on an NVIDIA RTX 3090 GPU, thereby enabling near real time inference. The framework can be seamlessly integrated with standard CT reconstruction pipelines, as ROI detection and RBAT segmentation can be executed alongside existing workflows without additional processing overhead. The effectiveness of the methodology was validated through comparative analysis against vacuum pycnometer measurements across multiple material classes. The proposed approach reduced porosity estimation deviation to within ± 3% for most materials, representing a clear improvement over traditional threshold only methods. The combined use of ROI detection, material classification, and adaptive thresholding resulted in more stable and repeatable porosity estimates, highlighting the robustness of the proposed pipeline.

While the method achieves high accuracy for trained and known material classes, reduced reliability was observed for unseen material types, indicating the need for further generalization. Future extensions involving broader material coverage and advanced adaptation strategies are expected to enhance applicability. Overall, the proposed framework offers an accurate, efficient, and automation friendly solution for porosity estimation, with strong potential for real time deployment across diverse industrial and materials science applications.

Data availability

All data analyzed during this study are available from author Prof. Sungwoo Park on reasonable request.

Received: 8 October 2025; Accepted: 6 February 2026

References

1. Lian, C., Zhuge, Y. & Beecham, S. The relationship between porosity and strength for porous concrete, Construction and Building Materials, Volume 25, Issue 11, Pages 4294–4298, ISSN 0950 – 0618. (2011). https://doi.org/10.1016/j.conbuildmat.2011.05.005
2. Bhupesh Goyal, A. & Pandey Critical review on porous material manufacturing techniques, properties & their applications, Materials Today: Proceedings, Volume 46, Part 17, 2021, Pages 8196–8203, ISSN 2214–7853. https://doi.org/10.1016/j.matpr.2021.03.163
3. Bossa, N. et al. Jerome Rose, Micro- and nano-X-ray computed-tomography: A step forward in the characterization of the pore network of a leached cement paste, cement and concrete research, **67**, Pages 138–147, ISSN 0008-8846, (2015). https://doi.org/10.1016/j.cemconres.2014.08.007
4. Hojat, N. et al. Automatic pore size measurements from scanning electron microscopy images of porous scaffolds. *J. Porous Mater.* **30**, 93–101. https://doi.org/10.1007/s10934-022-01309-y (2023).
5. Korat, L., Ducman, V., Legat, A. & Mirtic, B. Characterisation of the pore-forming process in lightweight aggregate based on silica sludge by means of X-ray micro-tomography (micro-CT) and mercury intrusion porosimetry (MIP), Ceramics International, Volume 39, Issue 6, Pages 6997–7005, ISSN 0272–8842, (2013). https://doi.org/10.1016/j.ceramint.2013.02.037
6. Augustine, U., Elinwa, M. & Umar X-ray diffraction and microstructure studies of gum Arabic-cement concrete, Construction and Building Materials, Volume 156, Pages 632–638, ISSN 0950 – 0618, (2017). https://doi.org/10.1016/j.conbuildmat.2017.08.162
7. Qsymah, A., Sharma, R., Yang, Z., Margetts, L. & Mummery, P. Micro X-ray computed tomography image-based two-scale homogenisation of ultra-high performance fibre reinforced concrete, construction and Building materials, **130**, Pages 230–240, ISSN 0950 – 0618, (2017). https://doi.org/10.1016/j.conbuildmat.2016.09.020
8. Wang, Y. S. & Dai, J. G. X-ray computed tomography for pore-related characterization and simulation of cement mortar matrix, **86**, Pages 28–35, ISSN 0963–8695, (2017). https://doi.org/10.1016/j.ndteint.2016.11.005
9. Zhang, H., Xu, B. S. Y. & Schlangen, E. Size effect on splitting strength of hardened cement paste: experimental and numerical study, cement and concrete composites, **94**, Pages 264–276, ISSN 0958–9465, (2018). https://doi.org/10.1016/j.cemconcomp.2018.09.018
10. Chung, S. Y., Kim, J. S., Stephan, D. & Han, T. S. Overview of the use of micro-computed tomography (micro-CT) to investigate the relation between the material characteristics and properties of cement-based materials, construction and Building materials, 229, 2019, 116843, ISSN 0950 – 0618. https://doi.org/10.1016/j.conbuildmat.2019.116843
11. Dong, H., Gao, P. & Ye, G. Characterization and comparison of capillary pore structures of digital cement pastes. *Mater. Struct.* **50, Issue 154**, https://doi.org/10.1617/s11527-017-1023-9 (2017).
12. Zelelew, H. M. & Papagiannakis, A. T. A volumetrics thresholding algorithm for processing asphalt concrete X-ray CT images. *Int. J. Pavement Eng.* **12** (Issue 16). https://doi.org/10.1080/10298436.2011.561345 (2011).
13. du Plessis, A. et al. Simple and fast porosity analysis of concrete using X-ray computed tomography. *Mater. Struct.* **49**, 553–562. https://doi.org/10.1617/s11527-014-0519-9 (2016).
14. Lu, H., Alymov, E., Shah, S. & Peterson, K. Measurement of air void system in lightweight concrete by X- ray computed tomography, Construction and Building Materials, Volume 152, Pages 467–483, ISSN 0950 – 0618, (2017). https://doi.org/10.1016/j.conbuildmat.2017.06.180
15. Niu, Y., Mostaghimi, P., Shabaninejad, M., Swietojanski, P. & Armstrong, R. T. Digital rock segmentation for petrophysical analysis with reduced user bias using convolutional neural networks. *Water Resour. Res.* **56** (Issue 2), Pages1–11. https://doi.org/10.1029/2019WR026597 (2019).
16. Jochen Hiller, P. & Hornberger Measurement accuracy in X-ray computed tomography metrology: toward a systematic analysis of interference effects in tomographic imaging. *Precis. Eng.* **45** https://doi.org/10.1016/j.precisioneng.2015.12.003 (2016). Pages 18–32, ISSN 0141–6359.
17. Arganda-Carreras, I. et al. *Trainable Weka Segmentation: a Machine Learning Toolfor Microscopy Pixel Classification* Vol. 33, Pages 2424–2426 (Bioinformatics, 2017). Issue 15https://doi.org/10.1093/bioinformatics/btx180

18. Chen, W. H. et al. A synchrotron-based local computed tomography combined with data-constrained modelling approach for quantitative analysis of anthracite coal microstructure. *J. Synchrotron Rad.* **21**, 586–593. https://doi.org/10.1107/S1600577514002793 (2014).
19. Menke, H. P. et al. 4D multi-scale imaging of reactive flow in carbonates: assessing the impact of heterogeneity on dissolution regimes using streamlines at multiple length scales, chemical geology, **481**, Pages 27–37, ISSN 0009–2541, (2018). https://doi.org/10.1016/j.chemgeo.2018.01.016
20. Garfi, G. et al. The sensitivity of estimates of multiphase fluid and solid properties of porous rocks to image processing. *Transp. Porous Med.* **131**, 985–1005. https://doi.org/10.1007/s11242-019-01374-z (2020).
21. Krizhevsky, A., Sutskever, I. & Hinton, G. E. Imagenet classification with deep convolutional neural networks. Advances in neural information processing systems, **25**, (2012).
22. Varfolomeev, I., Yakimchuk, I. & Safonov, I. *An Application of Deep Neural Networks for Segmentation of Microtomographic Images of Rock Samples* Vol. 8, 72 (Computers, 2019). Issue 4https://doi.org/10.3390/computers8040072
23. Wagner, A. et al. Permeability Estimation of regular porous structures: A benchmark for comparison of methods. *Transp. Porous Med.* **138**, 1–23. https://doi.org/10.1007/s11242-021-01586-2 (2021).
24. Schmidt, J. et al. Recent advances and applications of machine learning in solid-state materials science. *Npj Comput. Mater. Volume*. **5** (Issue 83). https://doi.org/10.1038/s41524-019-0221-0 (2019).
25. Kamrava, S., Tahmasebi, P. & Sahimi, M. Linking morphology of porous media to their macroscopic permeability by deep learning. *Transp. Porous Med.* **131**, 427–448. https://doi.org/10.1007/s11242-019-01352-5 (2020).
26. Taylr Cawte, A. & Bazylak Accurately predicting transport properties of porous fibrous materials by machine learning methods. *Electrochem. Sci. Adv.* **3** (Issue 1). https://doi.org/10.1002/elsa.202100185 (2022).
27. de Haan, K. et al. Resolution enhancement in scanning electron microscopy using deep learning. *Sci. Rep.* **9**, 12050. https://doi.org/10.1038/s41598-019-48444-2 (2019).
28. Szegedy, C., Vanhoucke, V., Ioffe, S., Shlens, J. & Wojna, Z. Rethinking the Inception Architecture for Computer Vision, *IEEE Conference on Computer Vision and Pattern Recognition (CVPR)*, Las Vegas, NV, USA, 2016, Pages 2818–2826, Las Vegas, NV, USA, 2016, Pages 2818–2826, (2016). https://doi.org/10.1109/CVPR.2016.308
29. Azimi, S. M. et al. Advanced steel microstructural classification by deep learning methods. *Sci. Rep.* **8, Issue 2128**, https://doi.org/10.1038/s41598-018-20037-5 (2018).
30. Bansal, A., Chen, X., Russell, B., Gupta, A. & Ramanan, D. Pixelnet: Representation of the Pixels, by the Pixels, and for the Pixels, ArXiv Prepr., ArXiv170206506. (2017).
31. Brian, L., DeCost, T., Francis, E. A. & Holm Exploring the microstructure manifold: image texture representations applied to ultrahigh carbon steel microstructures, acta materialia, **133**, Pages 30–40, ISSN 1359–6454, (2017). https://doi.org/10.1016/j.actamat.2017.05.014
32. Smith, J. D. et al. Quantitative Estimation of closed cell porosity in low density ceramic composites using X-ray microtomography. *Sci. Rep.* **13** (Issue 127). https://doi.org/10.1038/s41598-022-27114-w (2023).
33. Nickerson, S., Shu, Y., Zhong, D., Konke, C. & Tandia, A. Permeability of porous ceramics by X-ray CT image analysis, acta materialia, **172**, Pages 121–130, ISSN 1359–6454, (2019). https://doi.org/10.1016/j.actamat.2019.04.053
34. Graczyk, K. M. & Matyka, M. Predicting porosity, permeability, and tortuosity of porous media from images by deep learning. *Sci. Rep.* **10, Issue 21488**, https://doi.org/10.1038/s41598-020-78415-x (2020).
35. Graczyk, K. M., Strzelczyk, D. & Matyka, M. Deep learning for diffusion in porous media. *Sci. Rep.* **13, Issue 9769**, https://doi.org/10.1038/s41598-023-36466-w (2023).
36. Wu, H. et al. Predicting effective diffusivity of porous media from images by deep learning. *Sci. Rep.* **9, Issue 20387**, https://doi.org/10.1038/s41598-019-56309-x (2019).
37. Anderson, T. I. et al. 2D-to-3D image translation of complex nanoporous volumes using generative networks. *Sci. Rep.* **11** (Issue 20768). https://doi.org/10.1038/s41598-021-00080-5 (2021).
38. Buono, G. et al. Exploring microstructure and petrophysical properties of microporous volcanic rocks through 3D multiscale and super-resolution imaging. *Sci. Rep.* **13** (Issue 6651). https://doi.org/10.1038/s41598-023-33687-x (2023).
39. Zhang, H., Li, Y., Chen, Z., Wang, J. & Liu, Q. Geo segnet: A contrastive learning enhanced U net for geomaterial segmentation. *Trans. Mater. Res.* **3** https://doi.org/10.1016/j.tmater.2025.100049 (2025). Article 100049.
40. Alzubaidi, M., Mostaghimi, P., Armstrong, R. T. & Hoteit, H. Comparative assessment of U net based deep learning models for segmenting microfractures and pore spaces in digital rocks. *SPE Prod. Oper.* **39** https://doi.org/10.2118/215117-PA (2024).
41. AlRatrout, A., Bijeljic, B. & Blunt, M. J. Application of unsupervised deep learning to image segmentation and in situ contact angle measurements in a CO2 water rock system. *Adv. Water Resour.* **178** https://doi.org/10.1016/j.advwatres.2023.104385 (2023). Article 104385.
42. Zhang, Y., Wang, X., Yang, Z. & Chen, S. Deep learning based workflow for boundary and small target segmentation in digital rock images using UNet + + and IK EBM. *J. Petrol. Sci. Eng.* **214** https://doi.org/10.1016/j.petrol.2022.110596 (2022). Article 110596.
43. Wang, Y. D., Shabaninejad, M., Armstrong, R. T. & Mostaghimi, P. Physical accuracy of deep neural networks for 2d and 3d Multi-Mineral segmentation of rock MicroCt images. *Appl. Soft Comput. Volume*. **104** https://doi.org/10.1016/j.asoc.2021.107185 (2014).
44. Ge, M., Su, F., Zhao, Z. & Su, D. Deep learning analysis on microscopic imaging in materials science. *Mater. Today Nano*. **11**, 2588–8420. https://doi.org/10.1016/j.mtnano.2020.100087 (2020).
45. Sadegh Karimpouli, P. & Tahmasebi Segmentation of digital rock images using deep convolutional autoencoder networks, Computers & Geosciences, Volume 126, Pages 142–150, ISSN 0098-3004, (2019). https://doi.org/10.1016/j.cageo.2019.02.003
46. Ar Rushood, Ibrahim, Alqahtani, N. et al. Armstrong, RyanandSegmentation of X-Ray Images of Rocks Using Deep Learning. Paper presented at the SPE Annual Technical Conference and October (2020). https://doi.org/10.2118/201282-MS
47. Naif Alqahtani, F., Alzubaidi, R. T., Armstrong, P., Swietojanski, P. & Mostaghimi Machine learning for predicting properties of porous media from 2d X-ray images. *J. Petrol. Sci. Eng.* **184**, 0920–4105. https://doi.org/10.1016/j.petrol.2019.106514 (2020).
48. Sungwoo Park, M. C., Kang, Y., Oinam, A., Amoozegar, S. & Pyo Measurement of skeletal density and porosity of construction materials using a new proposed vacuum pycnometer, Measurement, 196, 2022, 111209, ISSN 0263–2241. https://doi.org/10.1016/j.measurement.2022.111209
49. Redmon, J. & Farhadi, A. YOLO9000: Better, Faster, stronger. *Proc. IEEE Conf. Comput. Vis. Pattern Recognit. (CVPR)*. 7263–7271. https://doi.org/10.1109/CVPR.2017.690 (2017).
50. Wang, C. Y., Bochkovskiy, A. & Liao, H. Y. M. YOLOv8: A high performance and efficient object detection model. *ArXiv Preprint*. **arXiv:2305.09972** https://doi.org/10.48550/arXiv.2305.09972 (2023).
51. Celebi, M. E., Kingravi, H. A. & Vela, P. A. A comparative study of efficient initialization methods for the k means clustering algorithm. *Pattern Recognit. Volume*. **46** (Issue 1), 200–210. https://doi.org/10.1016/j.patcog.2012.07.021 (2013).
52. Sezgin, M. & Sankur, B. Survey over image thresholding techniques and quantitative performance evaluation. *J. Electron. Imaging Volume*. **13** (Issue 1), 146–165. https://doi.org/10.1117/1.1631315 (2004).
53. Kaehler, A. & Bradski, G. Learning OpenCV 3: Computer Vision in C + + with the OpenCV Library. Computer Vision and Image Understanding. Volume 170, pp. 3–16. (2018). https://doi.org/10.1016/j.cviu.2018.01.003
54. Zhang, Y., Wang, Z., Li, X., Liu, Y. & Chen, H. Deep learning based semantic segmentation of pore structures in cement-based materials using X ray micro computed tomography. *Constr. Build. Mater.* **370** https://doi.org/10.1016/j.conbuildmat.2023.134812 (2023). Article 134812.

55. Li, H., Zhao, X., Wang, J. & Chen, Y. Semantic segmentation of complex pore structures in composite materials using deep learning and data augmentation. *Compos. B Eng.* **237** https://doi.org/10.1016/j.compositesb.2022.110096 (2022). Article 110096.

Author contributions

Conceptualization, Sungwoo Park and Yuvaraj Natarajan; Data curation, Sri Preethaa K.R., Danushkumar and Yuvaraj Natarajan; Formal analysis, Danushkumar and Yuvaraj Natarajan; Funding acquisition, Bubryur Kim; Methodology, Yuvaraj Natarajan and Danushkumar; Project administration, Sungwoo Park and Bubryur Kim; Resources, Sungwoo Park and Sukhoon Pyo; Software, Sri Preethaa K.R. and Danushkumar; Supervision, Bubryur Kim and Yuvaraj Natarajan; Validation, Sungwoo Park, Sukhoon Pyo and Bubryur Kim; Visualization, Yuvaraj Natarajan and Danushkumar; Writing – original draft, Sri Preethaa K.R. and Yuvaraj Natarajan; Writing – review & editing, Sri Preethaa K.R., Yuvaraj Natarajan and Sungwoo Park.

Funding

This work was supported by the National Research Foundation of Korea (NRF) grant funded by the Korea government (MSIT) (No. 2022R1C1C1005409). This research was supported by the Brain Pool program funded by the Ministry of Science and ICT through the National Research Foundation of Korea (NRF-2022H1D3A2A02082296). This work was supported by the National Research Foundation of Korea (NRF) grant funded by the Korea government (MSIT) (No. NRF-2018R1A5A1025137).

Declarations

Competing interests

The authors declare no competing interests.

Additional information

Correspondence and requests for materials should be addressed to S.P.K.

Reprints and permissions information is available at www.nature.com/reprints.